Friction and Diapycnal Mixing at a Slope: Boundary Control of Potential Vorticity

JESSICA BENTHUYSEN

Massachusetts Institute of Technology/Woods Hole Oceanographic Institution Joint Program, Woods Hole, Massachusetts, and CSIRO Marine and Atmospheric Research, and Centre for Australian Weather and Climate Research, Hobart, Tasmania, Australia

LEIF N. THOMAS

Department of Environmental Earth System Science, Stanford University, Stanford, California

(Manuscript received 29 July 2011, in final form 8 January 2012)

ABSTRACT

Although atmospheric forcing by wind stress or buoyancy flux is known to change the ocean's potential vorticity (PV) at the surface, less is understood about PV modification in the bottom boundary layer. The adjustment of a geostrophic current over a sloped bottom in a stratified ocean generates PV sources and sinks through friction and diapycnal mixing. The time-dependent problem is solved analytically for a no-slip boundary condition, and scalings are identified for the change in PV that arises during the adjustment to steady state. Numerical experiments are run to test the scalings with different turbulent closure schemes. The key parameters that control whether PV is injected into or extracted from the fluid are the direction of the geostrophic current and the ratio of its initial speed to its steady-state speed. When the current is in the direction of Kelvin wave propagation, downslope Ekman flow advects lighter water under denser water, driving diabatic mixing and extracting PV. For a current in the opposite direction, Ekman advection tends to restratify the bottom boundary layer and increase the PV. Mixing near the bottom counteracts this restratification, however, and an increase in PV will only occur for current speeds exceeding a critical value. Consequently, the change in PV is asymmetric for currents of the opposite sign but the same speed, with a bias toward PV removal. In the limit of a large speed ratio, the change in PV is independent of diapycnal mixing.

1. Introduction

Potential vorticity (PV) is a dynamical tracer whose large-scale spatial structure is important for understanding the ocean circulation (Holland et al. 1984; Rhines 1986). When isopycnals outcrop at the ocean's surface (e.g., Luyten et al. 1983) or intersect topography (e.g., Rhines 1998), boundary layer processes play a key role in determining the circulation's PV field. In the surface boundary layer, PV sources and sinks are determined by atmospheric forcing (Czaja and Hausmann 2009). In the bottom boundary layer (BBL), PV can be modified by mixing associated with internal wave breaking (e.g., Naveira Garabato et al. 2004; Saenko and Merryfield 2005), as well as frictional and diabatic processes that depend on the balanced flow and density fields. This coupling between the flow and nonconservative processes means that PV generation and extraction adjacent to topography is a complex problem. This work examines analytically and numerically the modification of PV in the BBL, which has not been fully explored with theory.

Previous theoretical studies have demonstrated how frictional and diabatic processes couple in setting the stratification over the slope. Bottom-enhanced diapycnal mixing weakens the stratification and also drives an upslope frictional flow (e.g., Phillips 1970; Wunsch 1970; Thorpe 1987). This flow tends to restratify the BBL by advecting denser water to shallower depths. Similarly, the frictional deceleration of a geostrophic current can drive a cross-isobath Ekman transport that modifies the stratification. In the latter case, horizontal density gradients develop and thermal wind shear weakens the near-bottom velocity, bottom stress, and Ekman transport (e.g., MacCready and Rhines 1991; Trowbridge and Lentz 1991).

Observations of the BBL in the abyssal ocean and on continental slopes indicate that diapycnal mixing and Ekman advection of buoyancy affect flows near

Corresponding author address: Jessica Benthuysen, CSIRO Marine and Atmospheric Research, GPO Box 1538, Hobart, Tasmania 7001, Australia.
E-mail: jessica.benthuysen@csiro.au

DOI: 10.1175/JPO-D-11-0130.1

topography. Near the Mid-Atlantic Ridge in the Brazil Basin, bottom-enhanced levels of turbulence mix the buoyancy field, tilting isopycnals downward toward the slope and driving diapycnal flows (St. Laurent et al. 2001). Observations off the northern California shelf show that upslope and downslope Ekman advection of buoyancy can lead to BBLs that are thin or thick, respectively (Lentz and Trowbridge 1991). Downslope Ekman advection of buoyancy advects lighter water under denser water, inducing convective mixing and isopycnal steepening within a bottom mixed layer (e.g., Moum et al. 2004). This frictional process has been used to explain the order 100-m-thick bottom mixed layers within deep western boundary currents of the Brazil Basin (Durrieu De Madron and Weatherly 1994).

Numerical studies have also revealed the potential importance of these boundary layer processes to the large-scale circulation. In wind-driven gyre simulations, Hallberg and Rhines (2000) and Williams and Roussenov (2003) examined how the inclusion of a sloping boundary modifies the PV of the circulation. Bottom frictional torques are more effective in changing PV at the boundary for a finite slope than for a wall with infinite slope (Hallberg and Rhines 2000; Williams and Roussenov 2003). Williams and Roussenov (2003) identify PV sinks from diapycnal mixing and downslope Ekman advection of buoyancy and a PV source from upslope Ekman advection of buoyancy. Diapycnal mixing tends to counteract local PV injection from an upslope Ekman transport and can dominate upslope Ekman transport in setting the buoyancy field (Williams and Roussenov 2003). These studies show that frictional and diabatic modification of PV is not confined to the boundaries. As the boundary currents separate from the coast, boundary-modified PV is transported into the gyre interior, creating PV gradients that tend to counteract eddy PV homogenization. These studies indicate that a metric is needed to evaluate the relative importance of diapycnal mixing and Ekman advection of buoyancy in the boundary modification of PV.

This work aims to quantify the PV sources and sinks that result from the coupling between diabatic and frictional processes at a slope. To this end, an analytical model is constructed to examine the time-dependent adjustment of a flow over a slope and the boundary processes that modify the PV field. In contrast to previous numerical studies, this analytical approach offers a more general means of quantifying the relative roles of these processes in controlling the PV field. In section 2, the model formulation, solution, and implications for PV dynamics are described. In section 3, the analytical solutions and scalings are tested using a numerical model with different turbulent closure schemes. The article is concluded in section 4.

2. Analytical model

a. Formulation

The simplest system to examine PV input or extraction in the bottom boundary layer is the frictional deceleration of a spatially uniform current along a boundary inclined at a constant angle to the horizontal in a fluid with initially constant stratification. The slope angle θ is assumed sufficiently small such that $\cos\theta \approx 1$ and $\sin\theta \approx \theta$. The density field, $\rho = \rho_b - \rho_o b/g$, is composed of a background density ρ_b, which has a constant buoyancy frequency N. Buoyancy b is the anomaly to the background density field and ρ_o is a reference density. The coordinate system is rotated such that the y direction is parallel to the slope and the z direction is normal to the slope. In this coordinate frame, the flow is composed of an along-isobath flow, u, in the x direction and a cross-isobath flow, v, in the y direction. The free surface tilt balances an along-isobath, geostrophic current of speed U. The flow has no along-isobath or cross-isobath variations. The flow w in the z direction is zero by the continuity equation and the no-normal-flow condition. The viscosity ν and the diffusivity κ are assumed constant. The flow's evolution is governed by the following equations:

$$\frac{\partial u}{\partial t} - fv = F^x = \frac{\partial}{\partial z}\left(\nu\frac{\partial u}{\partial z}\right), \tag{1}$$

$$\frac{\partial v}{\partial t} + f(u - U) + \theta b = F^y = \frac{\partial}{\partial z}\left(\nu\frac{\partial v}{\partial z}\right), \quad \text{and} \tag{2}$$

$$\frac{\partial b}{\partial t} - N^2\theta v = \mathcal{D} = \frac{\partial}{\partial z}\left(\kappa\frac{\partial b}{\partial z}\right), \tag{3}$$

where f is the constant planetary vorticity, F^x and F^y are the x and y components of the frictional force $\mathbf{F}$, and $\mathcal{D}$ consists of diabatic processes parameterized as buoyancy diffusion. At the initial time, the uniform current flows parallel to isobaths and the density field is ρ_b,

$$u = U \quad \text{at} \quad t = 0 \quad \text{and} \tag{4}$$

$$v = b = 0 \quad \text{at} \quad t = 0. \tag{5}$$

The equations are solved subject to the following no-slip and insulated boundary condition at the bottom and no change in the far-field flow and density field,

$$u = v = 0 \quad \text{at} \quad z = 0, \tag{6}$$

$$\frac{\partial b}{\partial z} + N^2 = 0 \quad \text{at} \quad z = 0, \tag{7}$$

$$u \to U \quad \text{as} \quad z \to \infty, \quad \text{and} \tag{8}$$

$$v, b \to 0 \quad \text{as} \quad z \to \infty. \tag{9}$$

Previous theoretical analyses have examined both cases $U \neq 0$ and the steady-state solution when U is not specified a priori. For $U \neq 0$, MacCready and Rhines (1991) solve (1)–(3) for approximate time-dependent solutions. In this case, the interior along-isobath flow sets up an Ekman flow within an inertial period, which has a cross-isobath transport $M_{\text{initial}} = U\delta_e/2$, where $\delta_e = (2\nu/f)^{1/2}$ is the Ekman layer depth. This Ekman transport advects buoyancy downslope (upslope) when the current is in (against) the direction of Kelvin wave propagation. Cross-isobath advection of buoyancy tilts the isopycnals and thermal wind shear reduces the bottom stress and Ekman transport. This process is known as buoyancy shutdown of the Ekman transport and occurs over a time $\mathcal{T}_{\text{shutdown,MR}} = (\sigma^{-1} + S)[S^2(1 + S)]^{-1}f^{-1}$ (MacCready and Rhines 1991), where the Prandtl number is $\sigma = \nu/\kappa$ and the slope Burger number is $S = (N\theta/f)^2$. Examples of slope Burger numbers on continental shelves range from 0.04 (northwest Africa) to 0.1–0.2 (northern California) to $O(1)$ (Oregon, Peru) (see Table 1 of Lentz and Chapman 2004). For typical slope angles and bottom stratification over midlatitude continental slopes where $S \ll 1$ and under the assumption that $\sigma \sim O(1)$, the time scale is

$$\mathcal{T}_{\text{shutdown}} = \sigma^{-1}S^{-2}f^{-1} \tag{10}$$

and buoyancy shutdown is a subinertial process. For long times, MacCready and Rhines (1991) show that the Ekman transport decays as $(t/\mathcal{T}_{\text{shutdown,MR}})^{-1/2}$ and approaches a steady-state solution.

The nonzero steady-state solution is best illustrated when $U = 0$. In this case, buoyancy diffusion tilts the isopycnals adjacent to the boundary in order to satisfy the insulated boundary condition in (7). This isopycnal tilt induces a cross-isobath pressure gradient and a frictional cross-isobath flow. For a nonrotating fluid, Phillips (1970) and Wunsch (1970) examine the steady-state balance between upslope advection of buoyancy and vertical diffusion of buoyancy. Thorpe (1987) extended Phillips's (1970) analyses to account for rotation and derived the following steady-state solution, where a small slope angle approximation is applied,

$$u = \frac{2M_{\text{Thorpe}}}{\delta_{\text{Thorpe}}}\left[1 - e^{-z/\delta_{\text{Thorpe}}}\cos\left(\frac{z}{\delta_{\text{Thorpe}}}\right)\right], \tag{11}$$

$$v = \frac{2M_{\text{Thorpe}}}{\delta_{\text{Thorpe}}}\left[e^{-z/\delta_{\text{Thorpe}}}\sin\left(\frac{z}{\delta_{\text{Thorpe}}}\right)\right], \tag{12}$$

$$b = N^2\delta_{\text{Thorpe}}\left[e^{-z/\delta_{\text{Thorpe}}}\cos\left(\frac{z}{\delta_{\text{Thorpe}}}\right)\right], \quad \text{and} \tag{13}$$

$$\delta_{\text{Thorpe}} = \delta_e(1 + \sigma S)^{-1/4}, \tag{14}$$

where $M_{\text{Thorpe}} = -\kappa/\theta$ is the cross-isobath transport that is directed upslope. In the limit of small-slope Burger numbers and order one Prandtl numbers, this steady-state solution occurs over an Ekman layer depth and the along-isobath flow asymptotes to

$$U_{\text{Thorpe}} = 2M_{\text{Thorpe}}/\delta_e \tag{15}$$

at the edge of the Ekman layer. This steady-state solution is for a spatially uniform diffusivity. When the diffusivity vertically varies, the cross-isobath transport is $M_{\text{Thorpe}} = -\kappa_\infty/\theta$, where κ_∞ is the diffusivity for $z/\delta_{\text{Thorpe}} \to \infty$ (Thorpe 1987).

Thus, for small-slope Burger numbers and order one Prandtl numbers, diffusion of buoyancy generates a steady-state upslope Ekman transport. This adjustment process can be described as buoyancy generation of the Ekman transport, a similar term to buoyancy shutdown of the initial Ekman transport, which emphasizes the role of buoyancy coupling with the frictional flow. Scaling arguments from (1)–(3) can be used to identify the time scale over which buoyancy generation occurs. In the limit of small-slope Burger numbers and order one Prandtl numbers, an upslope Ekman transport arises over a buoyancy generation time scale, where

$$\mathcal{T}_{\text{generation}} = \sigma^{-1}S^{-2}f^{-1}. \tag{16}$$

Hence, in this problem, buoyancy shutdown and generation occur over the same time scale.

Although the approximate time-dependent solution (MacCready and Rhines 1991) and steady-state solution (Thorpe 1987) yield insight into a current's frictional evolution at a slope, a full time-dependent solution is needed to quantify frictional and diabatic PV fluxes. In the following section, complete solutions are derived for the current's subinertial adjustment. These solutions show that, if the far-field flow is not equal to U_{Thorpe}, Thorpe's (1987) steady-state solution does not extend throughout the domain but is embedded within a boundary layer that is thicker than the Ekman layer. The solutions are used to study PV dynamics at a slope, in which this thicker boundary layer is necessary to estimate the total PV input or extraction.

b. Time-dependent solution

The time-dependent solutions to (1)–(3) are solved with initial and boundary conditions (4)–(9) following

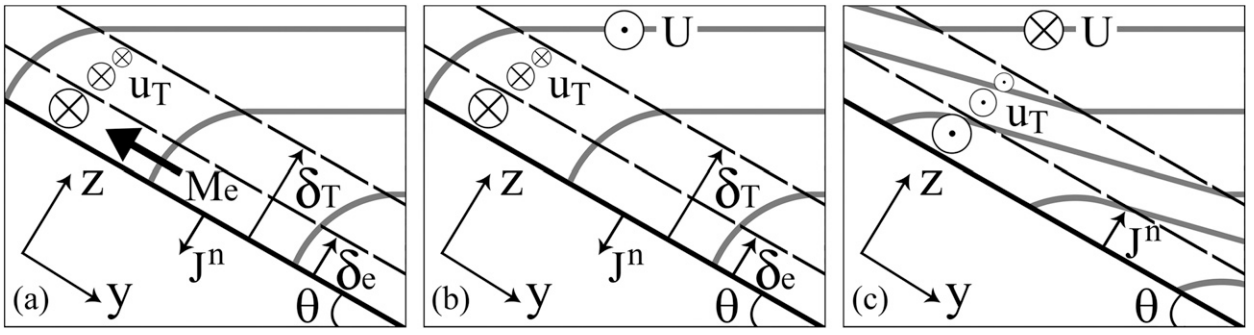

FIG. 1. (a) Buoyancy generation of the Ekman transport, $U = 0$. Diffusion of the stratification tilts the isopycnals (gray contours) normal to the boundary and forms a thermal boundary layer of depth δ_T that is thicker than an Ekman layer of depth δ_e. Diffusion of buoyancy leads to a positive outward PV flux J^n. The tilted isopycnals balance a thermal boundary layer flow u_T and generate an upslope Ekman transport M_e. (b) Buoyancy shutdown of the Ekman transport, $U > 0$ (in the direction of Kelvin wave propagation), downwelling. A geostrophic along-isobath flow U sets up a downslope Ekman transport within an inertial period. This Ekman transport advects buoyancy downslope, tilting isopycnals toward the slope and leading to a positive outward PV flux. The tilted isopycnals balance a vertically sheared geostrophic along-isobath flow u_T that opposes the interior geostrophic flow. Thus, as the total geostrophic flow goes to zero near the bottom, the Ekman transport weakens to zero. (c) Buoyancy shutdown of the Ekman transport, $U < 0$ (in the direction counter to Kelvin wave propagation), upwelling. The along-isobath flow U sets up an upslope Ekman transport within an inertial period. This Ekman transport advects buoyancy upslope, leading to a negative outward (positive inward) PV flux. The tilted isopycnals balance a flow, u_T, that opposes the interior geostrophic flow and weakens the upslope Ekman transport.

Thomas and Rhines (2002). The water column is split into the following three regions: an interior where viscous and diffusive effects are negligible, an Ekman layer of thickness δ_e where friction is of leading-order importance, and a diffusively growing boundary layer of thickness $(2\kappa t)^{1/2}$, which is referred to as a thermal boundary layer. Figure 1 illustrates the boundary layer decomposition for buoyancy generation (Fig. 1a) and buoyancy shutdown (Figs. 1b,c) of the Ekman transport. The adjustment is examined under the assumptions that slope Burger numbers are small, $S \ll 1$, and Prandtl numbers are order one, $\sigma = O(1)$. For subinertial dynamics the Ekman layer is embedded within a thermal boundary layer of depth δ_T, where $\delta_e/\delta_T \ll 1$. Variables are decomposed into contributions from three regions: that is, $u = u_i + u_T + u_e$, $v = v_i + v_T + v_e$, and $b = b_i + b_T + b_e$, where subscripts denote interior, thermal boundary layer, and Ekman layer components, respectively. In the interior, $u_i = U$ and $v_t = b_i = 0$ for all times, where the geostrophic, along-isobath flow is associated with a tilt in the free surface.

The variables are nondimensionalized by the following set of scalings:

$$u = |U_{\text{Thorpe}}|u', \quad v = |U_{\text{Thorpe}}|v', \quad b = N^2\delta_T b', \tag{17}$$

where primes denote nondimensional quantities. The along-isobath and cross-isobath speeds are nondimensionalized by the steady-state current speed in (15), and buoyancy is nondimensionalized by the buoyancy anomaly in the thermal boundary layer arising from the insulated boundary condition in (7). Time is nondimensionalized by $\mathcal{T}$, which is given by the buoyancy generation (16) and shutdown (10) time scale, that is, $t' = t/\mathcal{T}$. The coordinate normal to the boundary is nondimensionalized in the thermal boundary layer as $\xi' = z/\delta_T$, where $\delta_T = (2\kappa\mathcal{T})^{1/2} = \sigma^{-1}S^{-1}\delta_e$, and in the Ekman boundary layer as $\eta' = z/\delta_e$. In nondimensional form, (1)–(3) become

$$\sigma S^2\frac{\partial}{\partial t}(u_T + u_e) - (v_T + v_e) = \frac{1}{2}\left(\sigma^2 S^2\frac{\partial^2 u_T}{\partial\xi^2} + \frac{\partial^2 u_e}{\partial\eta^2}\right), \tag{18}$$

$$\sigma S^2\frac{\partial}{\partial t}(v_T + v_e) + (u_T + u_e) = -(b_T + b_e) + \frac{1}{2}\left(\sigma^2 S^2\frac{\partial^2 v_T}{\partial\xi^2} + \frac{\partial^2 v_e}{\partial\eta^2}\right), \quad \text{and} \tag{19}$$

$$\sigma S^2\frac{\partial}{\partial t}(b_T + b_e) - S(v_T + v_e) = \frac{1}{2\sigma}\left(\sigma^2 S^2\frac{\partial^2 b_T}{\partial\xi^2} + \frac{\partial^2 b_e}{\partial\eta^2}\right), \tag{20}$$

where the primes denoting nondimensional variables have been dropped. The boundary conditions (6)–(9) become (primes dropped)

$$\frac{U}{|U_{\text{Thorpe}}|} + u_T(\xi = 0) + u_e(\eta = 0) = 0, \tag{21}$$

$$v_T(\xi = 0) + v_e(\eta = 0), \tag{22}$$

$$\frac{\partial b_T}{\partial \xi}(\xi = 0) + \sigma^{-1}S^{-1}\frac{\partial b_e}{\partial \eta}(\eta = 0) + 1 = 0, \tag{23}$$

$$u_T, v_T, b_T \to 0 \quad \text{as} \quad \xi \to \infty, \quad \text{and} \tag{24}$$

$$u_e, v_e, b_e \to 0 \quad \text{as} \quad \eta \to \infty. \tag{25}$$

Next, the variables are expanded in powers of S in the thermal boundary layer as

$$u_T = \sum_{n=0}^{\infty} S^n u_T^{(n)}, \quad v_T = \sigma S^2 \sum_{n=0}^{\infty} S^n v_T^{(n)}, \quad \text{and}$$
$$b_T = \sum_{n=0}^{\infty} S^n b_T^{(n)}, \tag{26}$$

and in the Ekman layer as

$$u_e = \sum_{n=0}^{\infty} S^n u_e^{(n)}, \quad v_e = \sum_{n=0}^{\infty} S^n v_e^{(n)}, \quad \text{and}$$
$$b_e = \sigma S \sum_{n=0}^{\infty} S^n b_e^{(n)}. \tag{27}$$

The additional scale factors for v_T and b_e are motivated from (18) and (23), respectively. At $n = 0$, the governing equations describing the small slope Burger number dynamics are determined by substituting the expanded variables into (18)–(25) and collecting like orders of S. For notational simplicity, the $n = 0$ superscripts are dropped in the expressions below. In the thermal boundary layer, the $n = 0$ equations are

$$\frac{\partial u_T}{\partial t} - v_T = \frac{\sigma}{2}\frac{\partial^2 u_T}{\partial \xi^2}, \tag{28}$$

$$u_T = -b_T, \quad \text{and} \tag{29}$$

$$\frac{\partial b_T}{\partial t} = \frac{1}{2}\frac{\partial^2 b_T}{\partial \xi^2}. \tag{30}$$

For $\sigma = 1$, the thermal wind balance in (29) implies that $v_T = 0$. For $\sigma \neq 1$, the thermal wind balance is maintained by a cross-isobath flow $v_T \neq 0$. This cross-isobath flow is weaker than the Ekman flow by order σS^2 and is downslope for $\sigma > 1$. For $\sigma > 1$, the Coriolis acceleration associated with this downslope flow causes momentum to diffuse away from the boundary more slowly than in a nonrotating fluid. This process is described as "slow diffusion" of momentum (MacCready and Rhines 1991).

In the Ekman layer, the $n = 0$ equations are

$$-v_e = \frac{1}{2}\frac{\partial^2 u_e}{\partial \eta^2}, \tag{31}$$

$$u_e = \frac{1}{2}\frac{\partial^2 v_e}{\partial \eta^2}, \quad \text{and} \tag{32}$$

$$-v_e = \frac{1}{2}\frac{\partial^2 b_e}{\partial \eta^2}. \tag{33}$$

In (33), cross-isobath Ekman advection of the background density field balances diffusion of buoyancy. Buoyancy enters into the cross-isobath Ekman momentum equation (32) at order σS and is a higher-order correction to the leading-order dynamics.

The boundary conditions at $n = 0$ become

$$\frac{U}{|U_{\text{Thorpe}}|} + u_T(\xi = 0) + u_e(\eta = 0) = 0, \tag{34}$$

$$v_e(\eta = 0) = 0, \tag{35}$$

$$\frac{\partial b_T}{\partial \xi}(\xi = 0) + \frac{\partial b_e}{\partial \eta}(\eta = 0) + 1 = 0, \tag{36}$$

$$u_T, v_T, b_T \to 0 \quad \text{as} \quad \xi \to \infty, \quad \text{and} \tag{37}$$

$$u_e, v_e, b_e \to 0 \quad \text{as} \quad \eta \to \infty, \tag{38}$$

and all boundary layer variables are initially zero.

The flow in the thermal and Ekman boundary layers are coupled by boundary conditions (34) and (36). The key parameter controlling the flow's evolution is $U/|U_{\text{Thorpe}}|$. When the geostrophic flow near the bottom is nonzero, an Ekman flow is required to satisfy the no-slip condition (34). This Ekman flow produces a buoyancy anomaly b_e and forces the buoyancy field in the thermal boundary layer by (36). In the thermal boundary layer, buoyancy diffuses away from the boundary. By thermal wind balance, buoyancy diffusion adjusts u_T, which then feeds back onto the Ekman flow by (34). Closed form solutions to this coupled problem are obtained below.

The general form of the Ekman solution is

$$u_e = -\left[\frac{U}{|U_{\text{Thorpe}}|} + u_T(\xi = 0)\right] e^{-\eta}\cos\eta, \tag{39}$$

$$v_e = \left[\frac{U}{|U_{\text{Thorpe}}|} + u_T(\xi = 0)\right] e^{-\eta}\sin\eta, \quad \text{and} \tag{40}$$

$$b_e = -\left[\frac{U}{|U_{\text{Thorpe}}|} + u_T(\xi = 0)\right] e^{-\eta}\cos\eta \tag{41}$$

and is controlled by $U/|U_{\text{Thorpe}}|$ and u_T.

The time-dependent solution is determined by reducing the variables into a single equation for u_T. From (29) and (30), the along-isobath flow u_T satisfies the diffusion equation

$$\frac{\partial u_T}{\partial t} = \frac{1}{2}\frac{\partial^2 u_T}{\partial \xi^2}. \tag{42}$$

By applying (41) and (29) to (36), a single boundary condition (44) can be determined for u_T. Then, the diffusion equation is solved subject to the conditions

$$u_T(t = 0) = 0, \tag{43}$$

$$\frac{\partial u_T}{\partial \xi}(\xi = 0) - u_T(\xi = 0) = 1 + \frac{U}{|U_{\text{Thorpe}}|}, \quad \text{and} \tag{44}$$

$$u_T \to 0 \quad \text{as} \quad \xi \to \infty. \tag{45}$$

This equation is solved by using the Laplace transform $\tilde{U}_T(s,\xi) = \int_0^\infty u_T(t,\xi)e^{-st}\,dt$, where

$$\tilde{U}_T(s,\xi) = -\left(1 + \frac{U}{|U_{\text{Thorpe}}|}\right)\frac{e^{-\xi\sqrt{2s}}}{s(1 + \sqrt{2s})}. \tag{46}$$

By the inverse Laplace transform (Abramowitz and Stegun 1972) (details provided in the appendix), the solution to the along-isobath flow is

$$u_T(t,\xi > 0) = \left(1 + \frac{U}{|U_{\text{Thorpe}}|}\right) \times \left[\frac{e^{t/2}}{\sqrt{2\pi}}\int_0^t \left(\frac{\xi}{\tau} - 1\right)\frac{e^{-\tau/2 - \xi^2/(2\tau)}}{\sqrt{\tau}}\,d\tau - \frac{\xi}{\sqrt{2\pi}}\int_0^t \tau^{-3/2}e^{-\xi^2/(2\tau)}\,d\tau\right] \tag{47}$$

and

$$u_T(t,\xi = 0) = \left(1 + \frac{U}{|U_{\text{Thorpe}}|}\right) \times \left(-1 + e^{t/2} - \sqrt{\frac{2t}{\pi}} - \frac{e^{t/2}}{\sqrt{2\pi}}\int_0^t \tau^{1/2}e^{-\tau/2}\,d\tau\right). \tag{48}$$

Initially, $u_T(\xi = 0)$ is zero and in time asymptotes to

$$u_T(t \to \infty, \xi = 0) = -1 - \frac{U}{|U_{\text{Thorpe}}|}. \tag{49}$$

Solutions for the buoyancy anomaly, $b_T + b_e$, and the total along-isobath flow, $u = u_i + u_T + u_e$, are plotted in Fig. 2. When $U = 0$, diffusion of the stratification induces a positive buoyancy anomaly near the bottom and balances a negative along-isobath flow. When $U > 0$, buoyancy shutdown of an initial downslope Ekman transport increases this positive buoyancy anomaly through downslope advection of buoyancy. In time, the along-isobath flow reverses sign and tends to U_{Thorpe}. When $U < 0$, the upslope Ekman transport generates a negative buoyancy anomaly, which tends to counteract the positive buoyancy anomaly caused by diffusion of the stratification. In the special case $U/|U_{\text{Thorpe}}| = -1$, the two anomalies exactly cancel, thus yielding a buoyancy profile that does not change with time. In all cases, the along-isobath flow above the Ekman layer tends to U_{Thorpe}. This negative along-isobath flow extends into the interior as buoyancy diffuses away from the boundary.

The solution for u_T is used to calculate the dimensional Ekman transport M_e,

$$M_e = M_{\text{initial}} + |M_{\text{Thorpe}}|u_T(\xi = 0). \tag{50}$$

At the initial time, $M_e = M_{\text{initial}}$. By $t/\mathcal{T} = 1$, the Ekman transport has adjusted to 0.5 of its steady-state value. As shown in Fig. 3, the Ekman transport asymptotes to M_{Thorpe} for long times, regardless of the direction or strength of the initial along-isobath flow. Equations (48) and (50) can be used to show that the dimensional Ekman transport behaves as $M_{\text{Thorpe}} + (2/\pi)^{1/2}(M_{\text{initial}} + |M_{\text{Thorpe}}|)(t/\mathcal{T})^{-1/2}$ for long times. MacCready and Rhines (1991) found that the long-time behavior of the Ekman transport is $M_e = M_{\text{Thorpe}} + \mathcal{C}(M_{\text{initial}} + |M_{\text{Thorpe}}|)(t/\mathcal{T}_{\text{shutdown,MR}})^{-1/2}$. The constant $\mathcal{C}$ was empirically determined to equal 0.81 using numerical simulations (MacCready and Rhines 1991). Their solution is quantitatively consistent with the above solution because $(2/\pi)^{1/2} \approx 0.80$.

The solutions to the flow and buoyancy field are controlled by coupling between frictional and vertical mixing processes. Their evolution corresponds to changes in the PV field. In the next section, the analytical solution is used to quantify the contributions of these processes to the PV dynamics.

c. Potential vorticity dynamics

Convergences and divergences in the PV flux induce temporal changes to the PV field, that is,

$$\frac{\partial q}{\partial t} = -\nabla \cdot \mathbf{J}, \tag{51}$$

where $q = \omega_a \cdot \nabla B$ is the Ertel potential vorticity, $\nabla B = \nabla b + N^2\hat{\mathbf{z}}$ is the total buoyancy gradient, $\omega_a = f\hat{\mathbf{z}} + \nabla \times \mathbf{u}$ is the absolute vorticity, and $\hat{\mathbf{z}}$ is the vertical unit vector. The PV flux (Marshall and Nurser 1992),

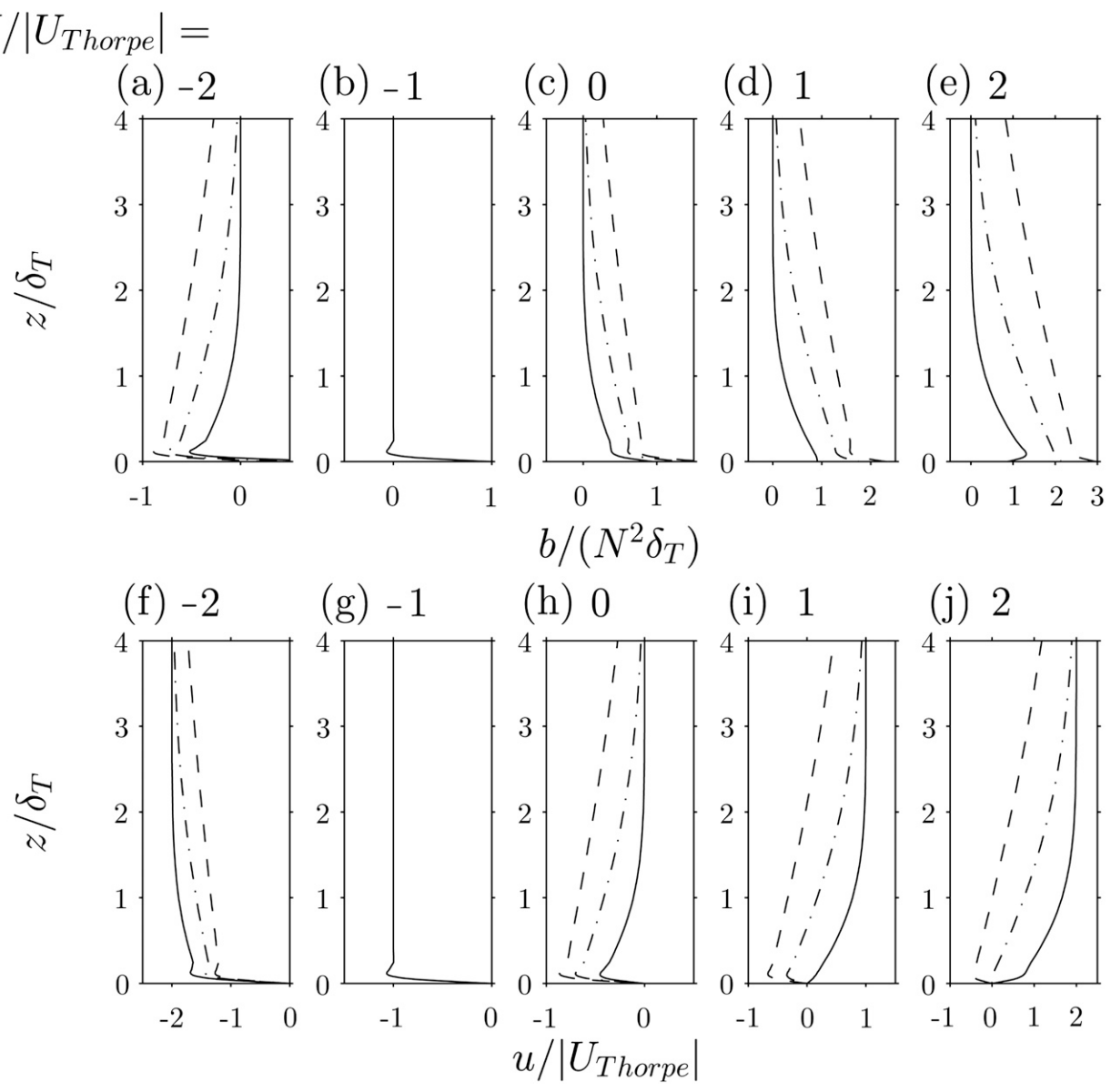

FIG. 2. (a)–(e) Analytical solution for the buoyancy and (f)–(j) the along-isobath flow evaluated at $t/\mathcal{T} = 1$ (solid), 5 (dashed–dotted), and 20 (dashed), with $S = 0.05$. The Ekman layer thickness is $\delta_e/\delta_T = 0.05$ in this example. Time is nondimensionalized by the buoyancy generation and shutdown time scale $\mathcal{T} = \sigma^{-1}S^{-2}f^{-1}$, (16) and (10).

$$\mathbf{J} = q\mathbf{u} + \nabla B \times \mathbf{F} - \mathcal{D}\omega_a, \tag{52}$$

is composed of advective PV fluxes, $\mathbf{J}_a = q\mathbf{u}$; frictional PV fluxes, $\mathbf{J}_F = \nabla B \times \mathbf{F}$; and diabatic PV fluxes, $\mathbf{J}_D = -\mathcal{D}\omega_a$. The analytical solution from the previous section is used to determine how the PV fluxes and anomalies depend on the key parameters of the problem.

A PV budget is constructed by vertically integrating (in the rotated coordinate system) (51). For a flow invariant in the along- and cross-isobath directions, lateral PV fluxes do not affect the budget. The upper limit of integration is at a height H, where the flow and stratification revert to their background values and vertical PV fluxes are negligibly small. Then, the PV budget becomes

$$\frac{dQ}{dt} = -(J_F^n + J_{\mathcal{D}}^n), \tag{53}$$

where $Q = \int_0^H q\,dz$ and J_F^n and $J_{\mathcal{D}}^n$ are the outward normal components of the frictional and diabatic PV fluxes, respectively, evaluated at the boundary. An outward positive PV flux reduces the vertically integrated PV

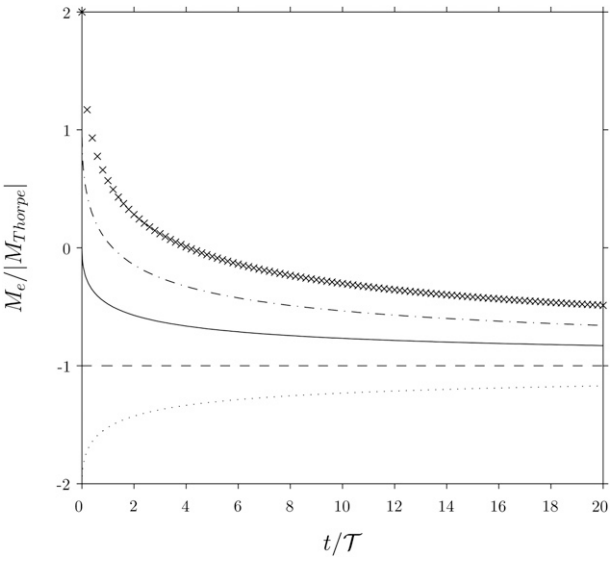

FIG. 3. The analytical solution for the Ekman transport for $U/|U_{\text{Thorpe}}| = -2$ (dotted), -1 (dashed), 0 (solid), 1 (dashed–dotted), and 2 (crisscrosses). The transport asymptotes to $-|M_{\text{Thorpe}}|$, regardless of its initial value.

(Figs. 1a,b), whereas an outward negative (i.e., inward positive) PV flux increases it (Fig. 1c). In the limit of small slope angles, these fluxes are

$$J_F^n = -N^2\theta\frac{\partial}{\partial z}\left(\nu\frac{\partial u}{\partial z}\right)\bigg|_{z=0} \quad \text{and} \tag{54}$$

$$J_{\mathcal{D}}^n = f\frac{\partial}{\partial z}\left(\kappa\frac{\partial b}{\partial z}\right)\bigg|_{z=0}. \tag{55}$$

For small slope Burger numbers and order one Prandtl numbers, these PV fluxes are

$$J_F^n = \left(\frac{fN^2\delta_T}{\mathcal{T}}\right)[(\sigma S)^{-1}v_e'(\eta = 0)] \quad \text{and} \tag{56}$$

$$J_{\mathcal{D}}^n = \left(\frac{fN^2\delta_T}{\mathcal{T}}\right)\left[\frac{1}{2}\frac{\partial^2 b_T'}{\partial\xi^2}\bigg|_{\xi=0} - (\sigma S)^{-1}v_e'(\eta = 0)\right] \tag{57}$$

(primes indicate nondimensional quantities for the $n = 0$ variables).

From (33), diffusion of buoyancy in the Ekman layer [the second term in (57)] is $O(\sigma^{-1}S^{-1})$ larger than diffusion of buoyancy in the thermal boundary layer. Diffusion is enhanced in the Ekman layer relative to the thermal boundary layer because δ_e is smaller than δ_T by a factor of σS. However, terms involving the Ekman flow in (56) and (57) cancel in the sum of the frictional and diabatic PV fluxes.

Using the $n = 0$ solution for b_T, the total PV flux, $J^n = J_F^n + J_{\mathcal{D}}^n$, is

$$J^n = \left(\frac{fN^2\delta_T}{\mathcal{T}}\right)\left(1 + \frac{U}{|U_{\text{Thorpe}}|}\right)\left[\sqrt{\frac{2}{\pi t'}} - e^{t'/2}\text{erfc}\left(\sqrt{\frac{t'}{2}}\right)\right]. \tag{58}$$

The term enclosed by square brackets is positive for all times. Thus, the parameter $U/|U_{\text{Thorpe}}|$ determines whether PV is input or extracted at the boundary; that is, the total outward PV flux is positive if $U/|U_{\text{Thorpe}}| > -1$, zero if $U/|U_{\text{Thorpe}}| = -1$, and negative if $U/|U_{\text{Thorpe}}| < -1$. Hence, J^n is asymmetric for along-isobath flows of opposite sign but equal strength. Buoyancy generation always extracts PV, whereas buoyancy shutdown extracts PV for $U > 0$ (downwelling favorable with a destratifying Ekman transport) and inputs PV for $U < 0$ (upwelling favorable with a stratifying Ekman transport). For long times, the total PV flux asymptotes to zero, so the change in the vertically integrated PV approaches a finite value.

The following expression for the change in the vertically integrated PV is determined from (1), (3), and (53)–(55):

$$\Delta Q \equiv Q(t) - Q(t = 0) = N^2\theta[u(t, z = 0) - u(t = 0, z = 0)] - fb(t, z = 0). \tag{59}$$

For no-slip boundary conditions, the term in parentheses is always zero, in which case the change in the vertically integrated PV is proportional to the buoyancy anomaly at the bottom. From the analytical solution, the change in the vertically integrated PV is

$$\Delta Q = fN^2\delta_T\left(1 + \frac{U}{|U_{\text{Thorpe}}|}\right) \times \left(-1 + e^{t'/2} - \sqrt{\frac{2t'}{\pi}} - \frac{e^{t'/2}}{\sqrt{2\pi}}\int_0^{t'}\tau^{1/2}e^{-\tau/2}\,d\tau\right). \tag{60}$$

For long times, the vertically integrated PV asymptotes to

$$\Delta Q_{t'\to\infty} = -fN^2\delta_T\left(1 + \frac{U}{|U_{\text{Thorpe}}|}\right). \tag{61}$$

The change in the steady state, vertically integrated PV is composed of a buoyancy anomaly, $N^2\delta_T = f|U_{\text{Thorpe}}|/\theta$,

TABLE 1. Numerical model parameters. The background diffusivity κ_∞ is equal to the background viscosity. All parameters below are calculated assuming constant mixing coefficients. The time scale $\mathcal{T}$ corresponds to $\mathcal{T}_{\text{generation}}$ and $\mathcal{T}_{\text{shutdown}}$, depending on whether U is zero or nonzero, and $\mathcal{T}_{\text{inertial}} = 2\pi/f$.

Configuration	U (cm s^{-1})	U/U_{Thorpe}	κ_∞ (10^{-5} m^2 s^{-1})	N^2 (10^{-5} s^{-2})	S	δ_e (m)	δ_T (m)	$\mathcal{T}/\mathcal{T}_{\text{inertial}}$
1 (high mixing and low N^2)	0	0	5.0	0.5	0.05	1.0	20.0	63.7
	±1.0	±1.0	5.0	0.5	0.05	1.0	20.0	63.7
	±2.0	±2.0	5.0	0.5	0.05	1.0	20.0	63.7
2 (low mixing and low N^2)	0	0	2.5	0.5	0.05	0.7	14.1	63.7
	±1.0	±1.4	2.5	0.5	0.05	0.7	14.1	63.7
	±2.0	±2.8	2.5	0.5	0.05	0.7	14.1	63.7
3 (high mixing and high N^2)	0	0	5.0	1.0	0.10	1.0	10.0	15.9
	±1.0	±1.0	5.0	1.0	0.10	1.0	10.0	15.9
	±2.0	±2.0	5.0	1.0	0.10	1.0	10.0	15.9

owing to diffusion of the stratification, and a buoyancy anomaly, $N^2\delta_T\, U/|U_{\text{Thorpe}}| = fU/\theta$, owing to buoyancy shutdown of the Ekman transport. A significant finding from this calculation is that these buoyancy anomalies are independent of stratification. This result occurs because density is vertically mixed over the thermal boundary layer depth, which varies inversely with N^2 over a buoyancy generation or shutdown time. Then, the resulting buoyancy anomaly $N^2\delta_T$ does not depend on the stratification. For both adjustment processes, increasing the slope angle leads to smaller steady-state buoyancy anomalies and less PV input or extracted because the time to reach steady state shortens. The relative contribution of these two processes to the net change in the vertically integrated PV is controlled by the parameter $U/|U_{\text{Thorpe}}|$. In the limit $U/|U_{\text{Thorpe}}| \gg 1$, the steady-state buoyancy anomaly associated with buoyancy shutdown dominates and the change in the vertically integrated PV is independent of vertical mixing coefficients. These predictions for the PV field's temporal evolution and steady state are tested using a numerical model.

3. Numerical experiments

A series of numerical experiments are run to test (i) the buoyancy generation time scale (16), (ii) the solution for ΔQ and its asymmetric dependence on the current's direction, and (iii) the sensitivity of the results to how mixing is parameterized.

The numerical model (used in Brink and Lentz 2010) solves the system of equations (1)–(3). No-buoyancy-flux and no-slip conditions are applied at the bottom. No-momentum-flux and no-buoyancy-flux conditions are applied at the top of the domain. The vertical domain is 350 m high with a vertical grid spacing of 20 cm. An implicit time stepping scheme is used with a time step of 8 s and the model is run at least 12 buoyancy generation or shutdown times.

The model parameters are motivated by midlatitude flows over continental slopes. Three configurations are considered and the parameters are summarized in Table 1. For all configurations, a slope angle of $\theta = 0.01$ and a Coriolis parameter of $f = 10^{-4}$ s^{-1} are assumed. In configuration 1, the parameters include $N^2 = 0.5 \times 10^{-5}$ s^{-2} and constant background mixing coefficients of $\kappa_\infty = \nu_\infty = 5 \times 10^{-5}$ m^2 s^{-1}. In configuration 2, the diffusivity and viscosity are reduced by half to test the buoyancy generation time scale's independence on the mixing coefficient. Reducing the mixing coefficient also increases the control parameter $U/|U_{\text{Thorpe}}|$ for a fixed U. Hence, this configuration also allows examination of the asymmetry in PV input versus PV extraction. In configuration 3, the initial stratification N^2 is doubled to examine $\mathcal{T}_{\text{generation}}$'s dependence on stratification and $\Delta Q_{t\to\infty}$'s independence of stratification. The model output is low-pass filtered with $0.1f$.

Two mixing schemes are applied. In the first scheme, the vertical diffusivity and viscosity are constant and equal to κ_∞. In the second scheme, mixing is dependent on the Richardson number Ri, where

$$\text{Ri} = \left(N^2 + \frac{\partial b}{\partial z}\right)\left[\left(\frac{\partial u}{\partial z}\right)^2 + \left(\frac{\partial v}{\partial z}\right)^2\right]^{-1} \tag{62}$$

and

$$\nu = \kappa = \begin{cases} \kappa_b, & \text{Ri} \le 0.2, \\ 10(\kappa_\infty - \kappa_b)(\text{Ri} - 0.2) + \kappa_b, & 0.2 < \text{Ri} < 0.3, \\ \kappa_\infty, & \text{Ri} \ge 0.3, \end{cases} \tag{63}$$

with $\kappa_b = 10^{-3}$ m^2 s^{-1}. This mixing scheme is similar to the vertical scheme applied in MacCready and Rhines (1993). The main impact of this mixing scheme is to thicken the bottom Ekman layer, which has implications

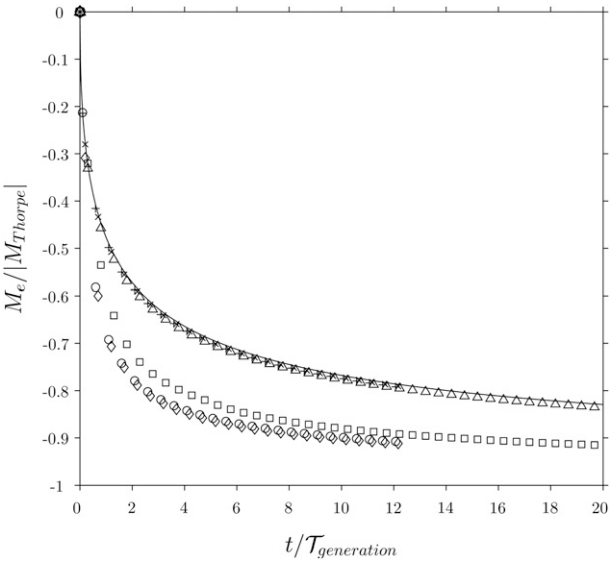

FIG. 4. The analytical (solid line) and numerical solutions for the Ekman transport during buoyancy generation (i.e., $U = 0$). The Ekman transport from simulations with constant diffusivities [pluses (configuration 1: high mixing and low N^2), crisscrosses (configuration 2: low mixing and low N^2), and triangles (configuration 3: high mixing and high N^2)], adjusts more slowly than M_e from simulations with Richardson number–dependent mixing coefficients [circles (configuration 1), diamonds (configuration 2), and squares (configuration 3)]. Time is nondimensionalized by (16) from the constant diffusivities.

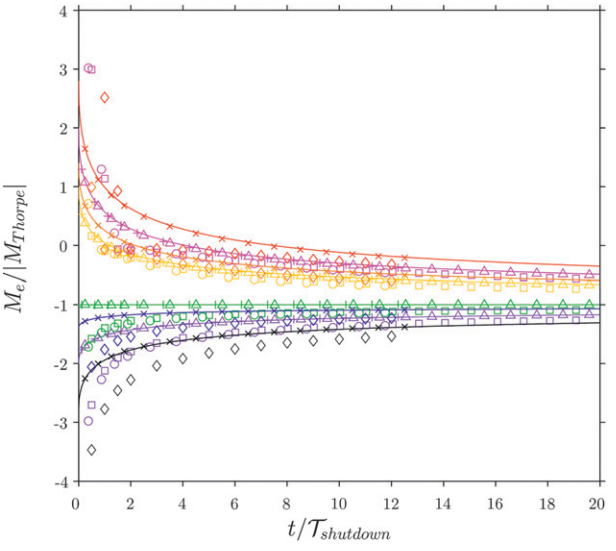

FIG. 5. Numerical and analytical solutions for the Ekman transport during buoyancy shutdown from all configurations, where $U/|U_{\text{Thorpe}}| = -2.8$ (black), -2 (purple), -1.4 (blue), -1 (green), 1 (yellow), 1.4 (orange), 2 (magenta), and 2.8 (red). The symbols are defined in Fig. 4 for simulations with constant and Richardson number–dependent mixing coefficients. Time is nondimensionalized by (10) from the constant diffusivities.

for the evolution and structure of the resulting flow, buoyancy, and PV fields.

a. Time-dependent evolution

The time evolution of the Ekman transport is shown in Fig. 4 for the buoyancy generation scenario, $U = 0$, and in Fig. 5 for buoyancy shutdown, $U \neq 0$. For $U = 0$ and constant mixing coefficients, the Ekman transport's time evolution is well predicted by the analytical solution. However, for the Richardson number–dependent mixing scheme, buoyancy generation tends to occur at a shorter time scale than $\mathcal{T}_{\text{generation}}$, (16).

This faster adjustment occurs for two reasons, a thickened Ekman layer and stronger initial buoyancy diffusion. First, for the vertically varying diffusivity, the Ekman layer is thicker relative to the simulations with constant diffusivity. Figure 6 shows an example of this thickening for $U = 0$, where profiles for $U \neq 0$ have a similar structure. For both mixing schemes, the steady-state Ekman transport is $M_e = (\nu \partial u/\partial z)|_{z=0}/f = -\kappa_\infty/\theta$. With bottom-enhanced mixing, the steady-state along-isobath speed is reduced in magnitude to maintain the same Ekman transport. From the thermal wind balance in (29), this weaker along-isobath speed corresponds to a weaker buoyancy anomaly compared to the constant diffusivity case. Thus, a smaller buoyancy anomaly is needed for the Ekman transport to reach steady state. Second, this buoyancy anomaly is generated through buoyancy diffusion. Because diffusion is bottom enhanced, a shorter time is needed to generate the buoyancy anomaly because mixing is more efficient.

For $U \neq 0$, the evolution of the Ekman transport with constant mixing coefficients is well predicted by the analytical solution. With the Richardson number–dependent mixing scheme, the initial Ekman transport is significantly increased by bottom-enhanced mixing because of the thicker Ekman layers. Rapid buoyancy shutdown can occur because cross-isobath buoyancy advection is enhanced by stronger Ekman transport. After approximately a shutdown time, the Ekman transport evolves more slowly to steady state.

b. Structure of the flow and buoyancy fields

The differences between the buoyancy and along-isobath flow for runs with vertically varying and constant mixing coefficients are illustrated in Fig. 7. Above the Ekman layer, the along-isobath flow approaches U_{Thorpe}, (15), for constant mixing. However, for bottom-enhanced mixing, the along-isobath speed is weaker than this scaling, which is consistent with the arguments presented above. For bottom-enhanced mixing, the buoyancy anomalies are always less than the

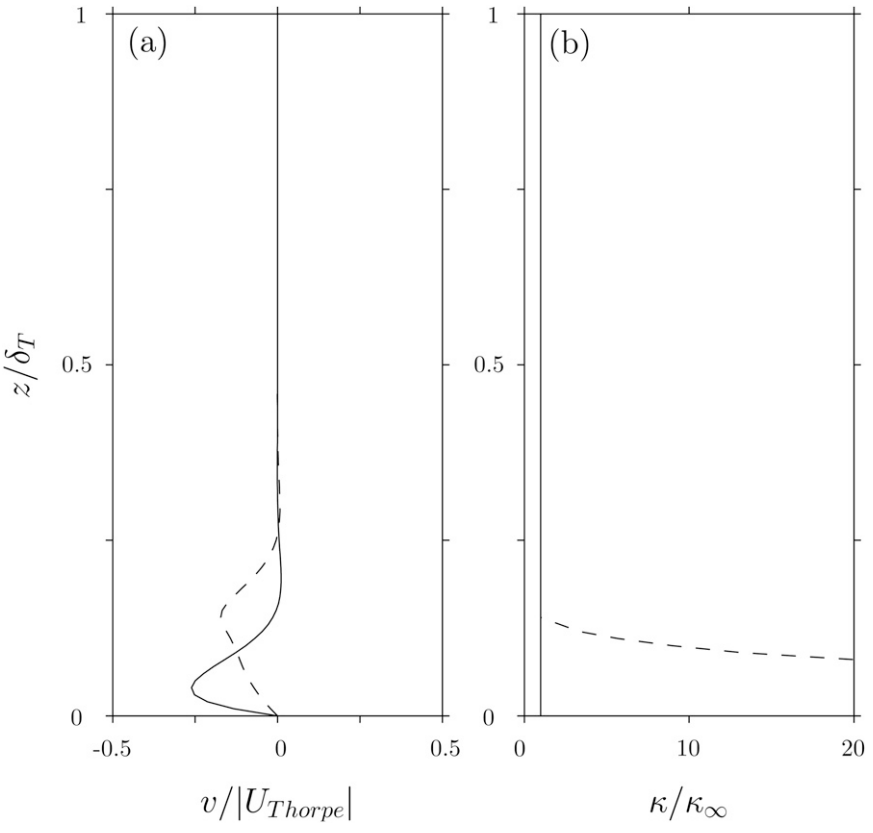

FIG. 6. The (a) cross-isobath flow and (b) vertical diffusivity from configuration 1: high mixing, low N^2, and $U/|U_{\text{Thorpe}}| = 0$, at 800 inertial periods. The vertical profiles are from constant (solid) and Richardson number–dependent mixing (dashed).

anomalies with constant diffusivity. The differences are more significant for simulations with upwelling, $U < 0$, versus downwelling, $U > 0$. This modification of the buoyancy field has implications for the PV field.

c. *Potential vorticity field*

The analytical solution in (61) predicts that PV is removed from the fluid even if there is no initial along-isobath current. PV is extracted by diffusion of buoyancy, which tilts the isopycnals to satisfy the no-buoyancy-flux boundary condition. For $U = 0$, time series for the change in the vertically integrated PV (Fig. 8) show that PV is indeed removed. However, the amount of PV extracted differs depending on the mixing scheme. With constant mixing coefficients, the numerical solutions tend to follow the analytical curve. The analytical solution tends to underestimate the amount of PV extracted because of an $O(S)$ correction to the buoyancy field that is not accounted for in (61). With Ri-dependent mixing, however, the amount of PV extracted is significantly less than predicted by analytical theory. This is a result of weaker buoyancy anomalies that arise when the mixing coefficients are bottom enhanced. For this mixing scheme, the difference between the analytical and numerical solutions is more sensitive to changes in stratification than background diffusivity κ_∞.

For $U \neq 0$, time series of the change in the vertically integrated PV (Fig. 9) show that there is again a good agreement between the analytical solution and the numerical simulations with constant mixing coefficients. For the Richardson number–dependent mixing scheme, there is a more rapid initial change in PV. This is because with this mixing scheme thicker Ekman layers and an intensified Ekman transport $\sim U\delta_e$ result, which leads to stronger buoyancy advection and a more rapid generation of PV anomalies. In time, buoyancy shutdown alone produces a steady-state PV anomaly $-f^2U/\theta$ that is independent of diapycnal mixing. Thus, the vertical variations in the diapycnal mixing modify the steady-state PV anomaly only through the buoyancy generation component $-f^2|U_{\text{Thorpe}}|/\theta$.

The vertically integrated PV anomalies evaluated at 800 inertial periods for all of the simulations are summarized in Fig. 10. These PV anomalies are compared to the analytical prediction for ΔQ evaluated at this time and at steady state, (61). A key finding from these

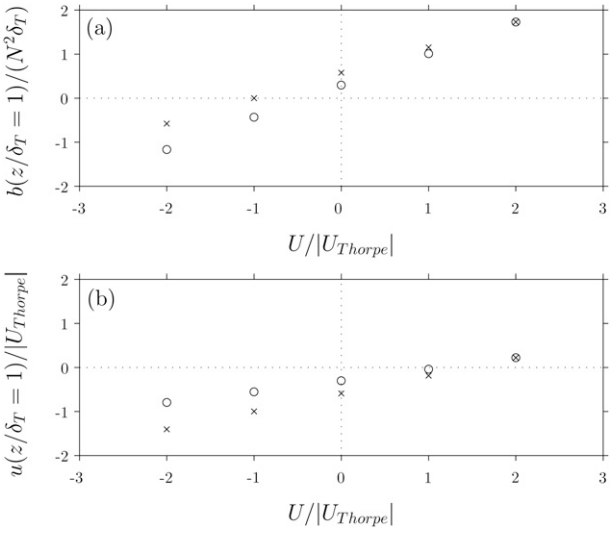

FIG. 7. The (a) buoyancy anomaly and (b) along-isobath flow at $z/\delta_T = 1$ at 800 inertial periods from configuration 1: high mixing and low N^2. The values are from constant (crisscrosses) or Richardson number–dependent mixing (circles).

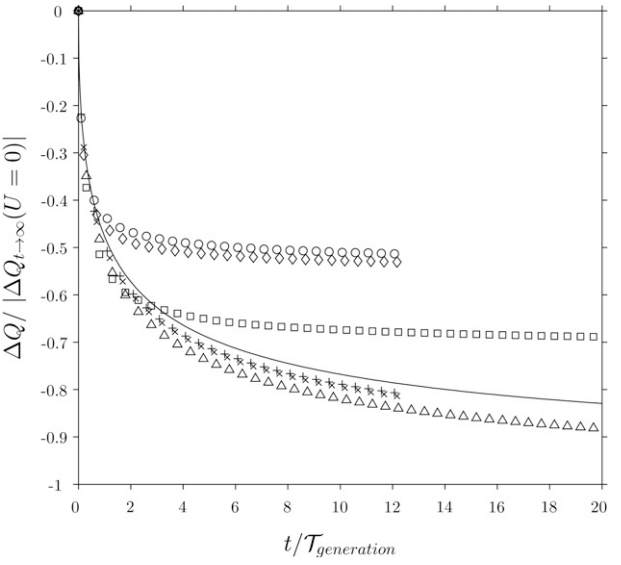

FIG. 8. The analytical (solid line) and numerical solutions for the change in the vertically integrated PV ΔQ for $U = 0$. The symbols are defined in Fig. 4 for simulations with constant and Richardson number–dependent mixing coefficients. The curves are normalized by $\Delta Q_{t\to\infty}(U = 0)$, (61), calculated using the background diffusivity κ_∞ of each respective configuration.

predictions is that the amount of PV extracted or input is asymmetric for a change in the sign of U. The model solutions for constant mixing coefficients capture this asymmetry and closely follow the analytical solution evaluated at 800 inertial periods. The deviation from the analytical solution at steady state in (61) is mainly due to the finite duration of the simulations.

For vertically varying mixing, the asymmetry in PV input and extraction is less pronounced. The asymmetry is caused by the buoyancy and PV anomalies that arise during buoyancy generation. In contrast to constant mixing, these buoyancy and PV anomalies are smaller with Ri-dependent mixing. The PV anomaly from buoyancy generation is proportional to the steady-state along-isobath flow, which depends on the Ekman layer depth [e.g., (15)]. A bound can be constructed for ΔQ assuming that the Ekman layer thickness is set by the maximum value of the diffusivity κ_b for the variable mixing scheme,

$$\frac{\Delta Q}{|\Delta Q_{t\to\infty}(U=0)|} = -\sqrt{\frac{\kappa_\infty}{\kappa_b}} - \frac{U}{|U_{\text{Thorpe}}|}, \qquad (64)$$

where the variables κ_∞, $\Delta Q_{t\to\infty}$, and U_{Thorpe} are from the constant mixing scheme. This bound, calculated with $\kappa_b = 10^{-3}$ m^2 s^{-1} and $\kappa_\infty = 5.0 \times 10^{-5}$ m^2 s^{-1}, is shown in Fig. 10. The Ri-dependent mixing solutions tend to fall between the analytical prediction for constant mixing coefficients (61) and the bound (64). Thus, for a no-slip boundary condition, bottom-enhanced mixing reduces the asymmetry in PV input versus extraction.

4. Conclusions

This study provides a theoretical framework for understanding the mechanisms that control the modification of PV in the deep ocean along sloping boundaries. The PV can only be changed by diabatic processes and frictional or nonconservative forces. In the bottom boundary layer, diabatic processes are primarily responsible for the change in PV yet are strongly influenced by friction through density advection by Ekman flows. Ekman flows generated by frictional deceleration of a current along a slope can result in the injection of PV into or removal of PV from the abyssal ocean depending on the direction and magnitude of the current.

Currents that flow in the direction of Kelvin wave propagation induce a downslope Ekman transport that advects lighter waters under denser waters, driving diapycnal mixing and extracting PV. Even in the absence of an imposed current, PV is extracted from the fluid as diapycnal mixing destratifies the boundary layer to satisfy the insulated slope boundary condition. Reversing the current direction results in an upslope Ekman transport that tends to restratify the boundary layer. However, this upslope Ekman transport only leads to a PV input if the current speed exceeds its steady-state value $|U_{\text{Thorpe}}|$, which is dependent on diapycnal mixing.

Only a finite amount of PV is extracted or input by this mechanism because a steady-state balance is reached.

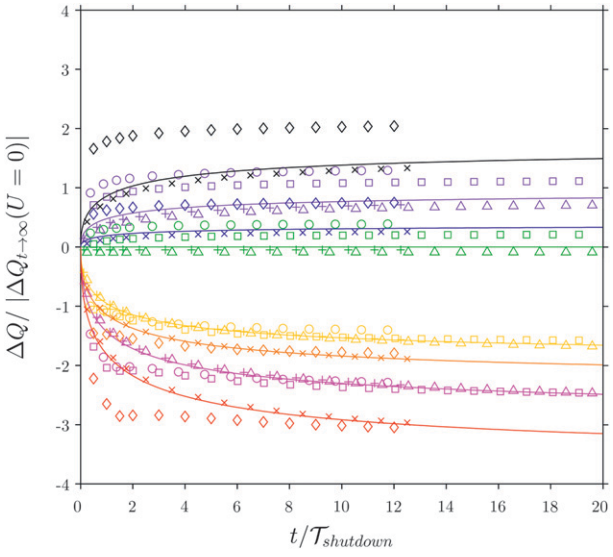

FIG. 9. The change in the vertically integrated PV during buoyancy shutdown from all configurations, where $U/|U_{\text{Thorpe}}| = -2.8$ (black), -2 (purple), -1.4 (blue), -1 (green), 1 (yellow), 1.4 (orange), 2 (magenta), 2.8 (red). The symbols are defined in Fig. 4.

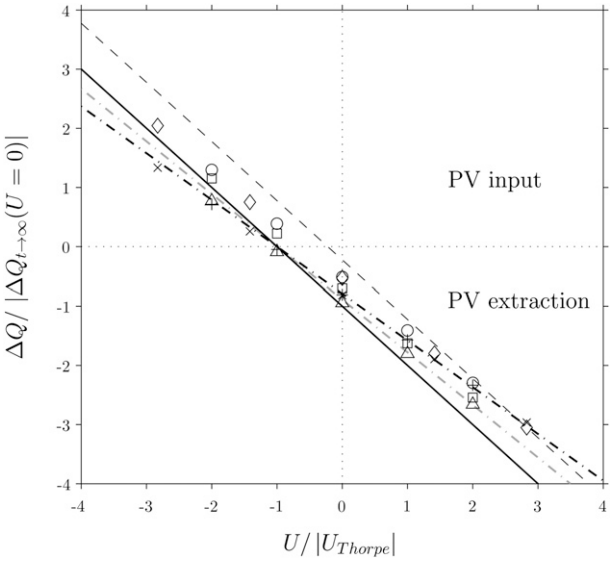

FIG. 10. The change in the vertically integrated PV ΔQ at 800 inertial periods from the analytical solution, with parameters from configurations 1 and 2 (dashed–dotted, black) and configuration 3 (dashed–dotted, gray), and the numerical simulations with constant diffusivities [pluses (configuration 1: high mixing and low N^2), crisscrosses (configuration 2: low mixing and low N^2), and triangles (configuration 3: high mixing and high N^2)] and Richardson number–dependent mixing coefficients [circles (configuration 1), diamonds (configuration 2), and squares (configuration 3)]. The steady-state scaling, $\Delta Q_{t\to\infty}$, for constant diffusivities, (61) (solid), and its upper bound for bottom-enhanced mixing, (64) (dashed), are also shown. The upper bound is calculated assuming $\kappa_\infty = 5.0 \times 10^{-5}$ m^2 s^{-1} and $\kappa_b = 10^{-3}$ m^2 s^{-1}.

A time-dependent analytical theory valid for small-slope Burger numbers, $S \ll 1$, is developed to quantify the net PV change resulting from this process. For times much longer than a buoyancy generation or shutdown time, the depth-integrated PV anomaly asymptotes to $\Delta\mathcal{Q}_{t\to\infty} = -(f^2/\theta)(U_{\text{Thorpe}} + U)$, a quantity that is independent of the stratification. The PV anomaly is asymmetric for a change in the direction of the initial along-isobath current U, because diffusion of the stratification caused by the insulating boundary condition tends to form low PV. In the limit $U/|U_{\text{Thorpe}}| \gg 1$, the difference between PV injection and removal for currents of the same magnitude but opposite direction is negligibly small and the change in the vertically integrated PV is independent of diapycnal mixing. Numerical experiments run with different vertical mixing schemes support these theoretical predictions. However, the PV's asymmetric response to a change in sign of U is less pronounced for Richardson number–dependent mixing coefficients. Bottom-enhanced mixing thickens the Ekman layer and weakens the steady-state speed and buoyancy anomaly. Thus, this mixing scheme reduces the amount of PV extracted from diffusion of the stratification alone.

This work shows that the deep ocean PV can be modified by processes in the bottom boundary layer. Some of the waters in the deep ocean originate in the surface mixed layer, where atmospheric forcing can drive a change in PV. The following question therefore arises: What are the relative roles of the two boundary layers in setting the PV of the abyss? To address this question, the PV fluxes are estimated and compared for surface and bottom boundary layers where deep waters outcrop. In regions of deep-water formation, buoyancy loss leads to a vertical diabatic PV flux that extracts PV from the fluid. Czaja and Hausmann (2009) estimate that, for an annual average, given the outcrop area in the North Atlantic of isopycnals spanning the range $26.5 < \sigma_\theta < 28$ kg m^{-3}, the diabatic PV flux associated with buoyancy loss is $\sim 10^{-14}$ m s^{-4}. The PV fluxes in the bottom boundary layer scale as $J^n \sim -\Delta\mathcal{Q}_{t\to\infty}/\mathcal{T}$. For midlatitude flows over continental slopes in the deep ocean (e.g., Durrieu De Madron and Weatherly 1994), $U + U_{\text{Thorpe}} \sim 0.1$ m s^{-1}, $\theta = 0.01$, and $N^2 \sim 1 \times 10^{-6}$ s^{-2}, yielding PV fluxes of $J^n \sim 10^{-15}$ m s^{-4}. Thus, the diabatic PV fluxes at the surface are larger than those at a sloping bottom. However, for a given isopycnal layer, the PV input or extracted depends on the surface integral of the PV fluxes. The area of deep-water formation is rather small compared to the area traced by deep western boundary currents as they traverse along continental slopes or ridges. Thus, boundary processes at sloping topography could play an important role in setting the deep ocean's PV field. Future studies should aim to quantify the

global impact of PV fluxes associated with bottom boundary layers and also consider the detachment of boundary-modified fluid (e.g., Armi 1978) and its transfer into the ocean interior.

Acknowledgments. We thank Ken Brink, who generously provided the original numerical model for the bottom boundary layer experiments. J. Benthuysen was supported by the MIT/WHOI Joint Program and CSIRO Marine and Atmospheric Research. Funding from Stanford University is also gratefully acknowledged. L. N. Thomas was supported by National Science Foundation Grant OCE-05-49699. The numerical experiments were run on the high performance computer of the Tasmanian Partnership for Advanced Computing at University of Tasmania.

APPENDIX

Thermal Boundary Layer Solution by Inverse Laplace Transform

In this appendix, steps involved in solving for u_T from (46) by inverse Laplace transform are provided. Equation (46) can be rewritten in the form

$$\tilde{U}_T(s,\xi) = \left(1 + \frac{U}{|U_{\text{Thorpe}}|}\right)\left\{\frac{1}{2a}\left[\frac{a}{(s-a)^2 - a^2}\right] - \frac{1}{\sqrt{2s}}\left[\frac{(s-a)+a}{(s-a)^2 - a^2}\right]\right\}e^{-\xi\sqrt{2s}}, \quad \text{(A1)}$$

where $a = 1/4$. The inverse Laplace transform of $\tilde{U}_T(s,\xi)$ is

$$u_T(t,\xi) = \mathcal{L}^{-1}\left[\tilde{U}_T(s,\xi)\right] = \frac{1}{2}\left(1 + \frac{U}{|U_{\text{Thorpe}}|}\right)\left\{\frac{1}{a}\mathcal{L}^{-1}[F_1]*\mathcal{L}^{-1}[F_3] - \sqrt{2}\mathcal{L}^{-1}[F_2]*\mathcal{L}^{-1}[F_4] - \sqrt{2}\mathcal{L}^{-1}[F_1]*\mathcal{L}^{-1}[F_4]\right\}, \quad \text{(A2)}$$

where the functions F_1, F_2, F_3, and F_4 are defined as follows and * denotes finite convolution. For functions $f(t)$ and $g(t)$, finite convolution is defined as $(f * g)(t) = \int_0^t f(t-\tau)g(\tau)\,d\tau$.

The inverse Laplace transforms of the above functions are (Abramowitz and Stegun 1972)

$$\mathcal{L}^{-1}[F_1] = \mathcal{L}^{-1}\left[\frac{a}{(s-a)^2 - a^2}\right] = e^{at}\sinh(at), \quad \text{(A3)}$$

$$\mathcal{L}^{-1}[F_2] = \mathcal{L}^{-1}\left[\frac{s-a}{(s-a)^2 - a^2}\right] = e^{at}\cosh(at), \quad \text{(A4)}$$

$$\mathcal{L}^{-1}[F_3] = \mathcal{L}^{-1}[e^{-c\sqrt{s}}] = \frac{c}{2\sqrt{\pi}}t^{-3/2}e^{-c^2/4t}, \quad \text{and} \quad \text{(A5)}$$

$$\mathcal{L}^{-1}[F_4] = \mathcal{L}^{-1}\left[\frac{e^{-c\sqrt{s}}}{\sqrt{s}}\right] = \frac{1}{\sqrt{\pi t}}e^{-c^2/4t}; \quad c = \xi\sqrt{2}. \quad \text{(A6)}$$

By applying finite convolution, the above functions can be used to determine (47) and (48).

REFERENCES

Abramowitz, M., and I. A. Stegun, 1972: *Handbook of Mathematical Functions*. Dover, 1046 pp.

Armi, L., 1978: Some evidence for boundary mixing in the deep ocean. *J. Geophys. Res.,* **83** (C4), 1971–1979.

Brink, K. H., and S. J. Lentz, 2010: Buoyancy arrest and bottom Ekman transport. Part I: Steady flow. *J. Phys. Oceanogr.,* **40,** 621–635.

Czaja, A., and U. Hausmann, 2009: Observations of entry and exit of potential vorticity at the sea surface. *J. Phys. Oceanogr.,* **39,** 2280–2294.

Durrieu De Madron, X., and G. Weatherly, 1994: Circulation, transport, and bottom boundary layers of the deep currents in the Brazil Basin. *J. Mar. Res.,* **52,** 583–638.

Hallberg, R., and P. Rhines, 2000: Boundary sources of potential vorticity in geophysical circulations. *IUTAM Symposium on Developments in Geophysical Turbulence,* Kluwer Academic Publishers, 51–65.

Holland, W. R., T. Keffer, and P. B. Rhines, 1984: Dynamics of the oceanic general circulation: The potential vorticity field. *Nature,* **308,** 698–705.

Lentz, S. J., and J. H. Trowbridge, 1991: The bottom boundary layer over the northern California shelf. *J. Phys. Oceanogr.,* **21,** 1186–1201.

——, and D. C. Chapman, 2004: The importance of nonlinear cross-shelf momentum flux during wind-driven coastal upwelling. *J. Phys. Oceanogr.,* **34,** 2444–2457.

Luyten, J. R., J. Pedlosky, and H. Stommel, 1983: The ventilated thermocline. *J. Phys. Oceanogr.,* **13,** 292–309.

MacCready, P., and P. B. Rhines, 1991: Buoyant inhibition of Ekman transport on a slope and its effect on stratified spin-up. *J. Fluid Mech.,* **223,** 631–661.

——, and ——, 1993: Slippery bottom boundary layers on a slope. *J. Phys. Oceanogr.,* **23,** 5–22.

Marshall, J. C., and A. J. G. Nurser, 1992: Fluid dynamics of oceanic thermocline ventilation. *J. Phys. Oceanogr.,* **22,** 583–595.

Moum, J. N., A. Perlin, J. M. Klymak, M. D. Levine, T. Boyd, and P. M. Kosro, 2004: Convectively driven mixing in the bottom boundary layer. *J. Phys. Oceanogr.,* **34,** 2189–2202.

Naveira Garabato, A. C., K. L. Polzin, B. A. King, K. J. Heywood, and M. Visbeck, 2004: Widespread intense turbulent mixing in the Southern Ocean. *Science,* **303,** 210–213.

Phillips, O. M., 1970: On flows induced by diffusion in a stably stratified fluid. *Deep-Sea Res.,* **17,** 435–443.

Rhines, P. B., 1986: Vorticity dynamics of the oceanic general circulation. *Annu. Rev. Fluid Mech.,* **18,** 433–497.

——, 1998: Circulation, convection and mixing in rotating, stratified basins with sloping topography. *Physical Processes in Lakes and Oceans,* J. Imberger, Ed., Amer. Geophys. Union, 209–226.

Saenko, O. A., and W. J. Merryfield, 2005: On the effect of topographically enhanced mixing on the global ocean circulation. *J. Phys. Oceanogr.,* **35,** 826–834.

St. Laurent, L. C., J. M. Toole, and R. W. Schmitt, 2001: Buoyancy forcing by turbulence above rough topography in the abyssal Brazil Basin. *J. Phys. Oceanogr.,* **31,** 3476–3495.

Thomas, L. N., and P. B. Rhines, 2002: Nonlinear stratified spin-up. *J. Fluid Mech.,* **473,** 211–244.

Thorpe, S. A., 1987: Current and temperature variability on the continental slope. *Philos. Trans. Roy. Soc. London,* **323A,** 471–517.

Trowbridge, J. H., and S. J. Lentz, 1991: Asymmetric behavior of an oceanic boundary layer above a sloping bottom. *J. Phys. Oceanogr.,* **21,** 1171–1185.

Williams, R. G., and V. Roussenov, 2003: The role of sloping sidewalls in forming potential vorticity contrasts in the ocean interior. *J. Phys. Oceanogr.,* **33,** 633–648.

Wunsch, C., 1970: On oceanic boundary mixing. *Deep-Sea Res.,* **17,** 293–301.